

# Effect of Growth Rate on the Microstructure and Microhardness in a Directionally Solidified Al-Zn-Mg Alloy



EMINE ACER, EMIN ÇADIRLI, HARUN EROL, and MEHMET GÜNDÜZ

The Al-5.5Zn-2.5Mg (wt pct) ternary alloy was prepared using a vacuum melting furnace and a casting furnace. Five samples were directionally solidified upwards at a constant temperature gradient ( $G = 5.5$  K/mm) under different growth rates ( $V = 8.3\text{--}165$   $\mu\text{m/s}$ ) in a Bridgman-type directional solidification furnace. The primary dendrite arm spacing,  $\lambda_1$ , secondary dendrite arm spacing,  $\lambda_2$ , and microhardness, HV, of the samples were measured. The effects of  $V$  on  $\lambda_1$ ,  $\lambda_2$  and HV properties of the Al-Zn-Mg alloy were studied by microstructure analysis and mechanical characterization. Microstructure characterization of the alloys was carried out using optical microscopy, scanning electron microscopy, wavelength-dispersive X-ray fluorescence spectrometry, and energy dispersive X-ray spectroscopy. From the experimental results, it is found that the  $\lambda_1$ ,  $\lambda_2$  values decrease, but HV values increase with the increase in  $V$ , and HV values decrease with the increase in  $\lambda_1$  and  $\lambda_2$ . Dependencies of dendritic spacing and microhardness on the growth rate were determined using linear regression analysis. The growth rate, microstructure, and Hall-Petch-type relationships obtained in this work have been compared with the results of previous studies.

DOI: 10.1007/s11661-016-3484-9

© The Minerals, Metals & Materials Society and ASM International 2016

## I. INTRODUCTION

THE increased demand on reducing vehicle weight in the automotive industry, aircraft, and aerospace system has raised the need to develop improved structural materials. These materials are required to be stronger, lighter, and maintain good mechanical properties at elevated temperatures. Therefore, low density, oxidation resistance, and high strength metallic compounds with increased reliability at higher stress levels have been developed.

Pure aluminum is soft and lacks strength, but when alloyed with small amounts of nickel, silicon, copper, zinc, magnesium or other elements, it displays a variety of useful properties. Al-Zn-Mg (7xxx alloys)-based cast alloys are excellent candidate materials for such applications due to their light weight, good castability, high mechanical properties, and excellent corrosion resistance in most environments. Such alloys are widely used in automobile applications due to their high strength-to-weight ratio and their technological importance as medium to high strength

materials.<sup>[1-6]</sup> The microstructure and mechanical properties obtainable from these alloys are known to be influenced by the growth rate, addition of the alloying elements, and heat treatment procedures.

Since strength and hardness of alloys mainly depend on their microstructure, a lot of efforts have been made for refining microstructure of casting in order to improve mechanical properties of Al alloys. Power ultrasound,<sup>[7]</sup> electromagnetic stirring,<sup>[8,9]</sup> adding modifier, and refiner<sup>[10,11]</sup> have been used to refine microstructure of alloys. However, there has been little research on refining the microstructure by improving the bulk melt's cooling rate. In the Bridgman-type solidification, the cooling rate,  $\dot{T}$  is given as ( $\dot{T} = GV$ ), where  $G$  is the temperature gradient in the solid-liquid interface and  $V$  is the growth rate of solid-liquid interface.  $\dot{T}$  is linearly proportional to  $V$  for a given  $G$ . Growth rate, and  $G$  can be controlled independently and measured accurately, so thus,  $\dot{T}$ , by Bridgman-type solidification. Areas of directionally solidified alloy that tend to grow faster have finer microstructures and better mechanical properties as compared to the slowly grown ones. For the samples with higher growth rate, the deposition of the partially soluble compounds at the boundaries is much less; hence, these areas have better mechanical properties.<sup>[12]</sup> Under steady-state growth, with well-controlled experimental conditions, the alloys solidify with planar solid-liquid interfaces when the growth rate is below the critical growth rate. If the growth rate is increased above the critical growth rate, the first stage in the breakdown of the interface is the formation of a cellular structure. Cellular microstructures are only stable for a certain range of growth rates. At

EMINE ACER, Postdoctoral Researcher, is with the Department of Physics, Institute of Science, Erciyes University, Kayseri, Turkey. EMIN ÇADIRLI, Professor, is with the Department of Physics, Faculty of Arts and Sciences, Niğde University, Niğde, Turkey. HARUN EROL, Ph.D. Student, is with the Department of Physics, Institute of Science, Erciyes University, Kayseri, Turkey and also with the Karatekin University Faculty of Arts and Sciences, Department of Physics, Çankiri, Turkey. MEHMET GÜNDÜZ, Professor, is with Erciyes University, Faculty of Science, Department of Physics, Kayseri, Turkey. Contact e-mail: gunduz@erciyes.edu.tr

Manuscript submitted October 19, 2015.

Article published online April 8, 2016

sufficiently high growth rates, the cells or primary arms of solid develop secondary arms, *i.e.*, dendrites form. Dendrite arm spacings decrease with increasing growth rate, because higher growth rate allows less time for lateral diffusion of the rejected solute and therefore requires smaller dendrite arm spacings.<sup>[13]</sup>

Dendritic growth is perhaps the most frequently observed phenomenon during the solidification whose morphology is characterized by primary ( $\lambda_1$ ), secondary ( $\lambda_2$ ) and tertiary ( $\lambda_3$ ) dendrite arm spacings. As the fluid flow in the interdendritic channels depends on these dendrite arm spacings, it is important to know the variation of these parameters during the solidification process to analyze microsegregation pattern which influences for instance the homogenization kinetics, ultimate tensile strength, ductility, toughness, and yield tensile strength of solidified alloys.<sup>[14–16]</sup> It is well known that dendrite fineness can be of even more importance than the grain size for the improvement of mechanical properties. Therefore, these structures can be considered as an important object of investigation with respect to the directional solidification of metallic alloys. A number of directional solidification studies have been reported in the last decades to point out the effect of microstructure upon the mechanical properties, most studies have shown that for steady or unsteady growth conditions, the primary dendrite arm spacings decrease as the growth rate or temperature gradient increases.<sup>[17–20]</sup>

The first significant treatment to characterize  $\lambda_1$  as a function of  $V$ ,  $G$ , and  $C_0$  was developed by Hunt.<sup>[21]</sup> Assuming that the region close to the tip can be approximated as part of sphere and using the mass balance condition, Hunt obtained  $\lambda_1$  as follows:

$$\lambda_1 = 2.83[m(k-1)D\Gamma]^{0.25} C_0^{0.25} G^{-0.50} V^{-0.25}, \quad [1]$$

where  $m$  is the liquidus slope,  $\Gamma$  is the Gibbs–Thomson coefficient,  $k$  is the solute partition coefficient, and  $D$  is the liquid solute diffusivity. Trivedi<sup>[22]</sup> modified Hunt's model,<sup>[21]</sup> using marginal stability criterion, and obtained

$$\lambda_1 = 2.83[m(k-1)D\Gamma L]^{0.25} C_0^{0.25} G^{-0.50} V^{-0.25}, \quad [2]$$

where  $L$  is a constant depending on harmonic perturbations. According to Trivedi,<sup>[22]</sup>  $L$  can be any value between 10 and 28 for dendritic growth. Kurz and Fisher<sup>[23]</sup> assumed the shape of the dendrite tip ellipsoids, and using the marginal stability criterion for an isolated dendrite, they obtained

$$\lambda_1 = 4.3[m(k-1)D\Gamma/k^2]^{0.25} C_0^{0.25} G^{-0.50} V^{-0.25}. \quad [3]$$

Also, Okamoto and Kishitake<sup>[24]</sup> have proposed a simplified method for correlating primary dendrite spacing with solidification parameters. They have assumed the secondary dendrite arms to be plates that become thicker as the solidification goes on. Briefly, all kinds of the above models can be summarized as  $\lambda_1 = k_x C_0^a G^{-b} V^{-c}$ , and the difference between them is the constants  $k_x$  only. That is because  $\lambda_1$  obtained for the dilute binary alloys in the steady-state growth conditions and convections was ignored.

The size of secondary dendrite arm spacings depends on many factors such as liquid metal treatment, temperature gradient, growth rate/solidification time, and chemical composition of melt. Among them the growth rate/solidification time have dominant impacts. It is well known that the microstructural scale significantly affects the mechanical properties of metallic materials. Under steady-state growth for the constant  $C_0$  and  $G$ ,  $V$  can be controlled independently and measured accurately and  $\lambda_2$  obtained accurately as a function of  $V$ . The variation in  $\lambda_2$  for small Peclet number conditions given by Trivedi and Somboonsuk<sup>[25]</sup> was obtained as

$$\lambda_2 = \left( \frac{8\Gamma DL}{kV\Delta T_0} \right)^{0.5}, \quad [4]$$

where  $\Delta T_0$  is the difference between the liquidus and solidus equilibrium temperatures.

From this equation,  $\lambda_2$  can be expressed as of  $V$ :

$$\lambda_2 = k_{TS} V^{-0.5}. \quad [5]$$

Bouchard–Kirkaldy<sup>[26]</sup> obtained  $\lambda_2$  by a Mullis and Sekerka<sup>[27]</sup> type formula proved from the start to be adequate in both unsteady- and steady-state heat flows, and so it recommends itself in calibrated form:

$$\lambda_2 = 2\pi a_2 \left( \frac{4\Gamma}{C_0(1-k)^2 T_F} \left( \frac{D}{V} \right)^2 \right)^{0.33}, \quad [6]$$

where  $a_2$  is the secondary dendrite-calibrating factor, which depends on the alloy composition, and  $T_F$  is the fusion temperature of the solvent. From this equation,  $\lambda_2$  can be written as a function of  $V$ :

$$\lambda_2 = k_{BK} V^{-0.66}. \quad [7]$$

As can be seen from Eqs. [1] through [3], exponent value of  $V$  for  $\lambda_1$  is 0.25, and exponent values of  $V$  for  $\lambda_2$  changes from 0.5 to 0.66 from Eqs. [4] through [7].

Over the range of conventional grain sizes ( $\mu\text{m}$  scales), the values of mechanical properties (namely yield strength ( $\sigma$ ), hardness (HV)) increase with the decreasing of the grain size ( $d$ ). The relationship between yield strength or hardness and grain size of the conventional polycrystalline metallic materials are described by the Hall–Petch<sup>[28,29]</sup>-type equation. The Hall–Petch type relationship between the microhardness and the grain size can be expressed as follows:

$$\text{HV} = \text{HV}_0 + k_1 d^{-0.5}, \quad [8]$$

where  $\text{HV}_0$  is the initial microhardness of equilibrated phase and  $k_1$  is a constant which depend on kind of materials. In the present study, the mean grain size can be the primary dendrite arm spacing,  $\lambda_1$ , and the secondary dendrite arm spacing,  $\lambda_2$ . Thus, the microhardness and the dendritic spacings can be expressed as follows:

$$\text{HV} = \text{HV}_0 + k_2 \lambda_1^{-0.50}, \quad [9]$$

$$HV = HV_0 + k_3 \lambda_2^{-0.50}, \quad [10]$$

where  $k_2$  and  $k_3$  are constants which depend on kind of materials.  $HV_0$ ,  $k_2$ , and  $k_3$  can be experimentally determined.

In Eq. [9], using  $\lambda_1$  value, and in Eq. [10], using  $\lambda_2$  values, the relationships between microhardness and the growth rate can be obtained ( $\lambda_1 = A \cdot V^{-0.25}$  from Eqs. [1] through [3] and  $\lambda_2 = B \cdot V^{-(0.50-0.66)}$  from Eqs. [4] through [7]) as follows:

$$HV = HV_0 + k_4 V^n, \quad [11]$$

where  $n$  is the exponent value of  $V$  which changes from 0.125 to 0.33. A set of the samples that are used for microhardness measurement need to have similar grain size and shape, and temperature. Strength will increase with grain size reduction only if the reduction of small grains does not increase the amount of microporosity, the percentage value of second phase, or the dendrite spacing.<sup>[30]</sup> Materials with very different grain size distributions will obey slightly different forms of the Hall–Petch relation<sup>[31]</sup>. When the grain sizes at the materials are very small ( $\leq 10$  nm), the Hall–Petch relation no longer applies, because for the very small grains, the dominant deformation mechanism will change from transgranular slip to grain boundary sliding and very small grain cannot support distributions of dislocations.<sup>[32,33]</sup> The grain size distribution, the strain rate, the temperature, and the grain boundary distribution affect the mechanical properties (*i.e.*, microhardness, tensile strength, yield strength) of the materials.

Materials processed *via* directional solidification tend to show advantages of reduced microsegregation, microvoids and amount of microporosity, refined and more uniform microstructure.<sup>[34–36]</sup> In the directional solidification, the solidification parameters ( $C_0$ ,  $V$ ,  $G$ ,  $\dot{T}$ ) directly affect the microstructure parameters ( $\lambda_1$ ,  $\lambda_2$ ) of the alloy and thus significantly influence their mechanical properties. Expressions correlating the mechanical properties with grain sizes ( $\lambda_1$ ,  $\lambda_2$ ) are useful for a previous planning of a solidification (casting) conditions in terms of a determined level of mechanical behaviors. Therefore, correlating the microhardness, yield strength, ultimate tensile strength, growth rates, dendritic spacings, and solidification processing variable of the Al–Zn–Mg alloy will be useful.

However, few systematic investigation have been performed on the Hall–Petch relationship, particularly regarding the hardness on the dendritic grain sizes ( $\lambda_1$ ,  $\lambda_2$ ) and growth rate ( $V$ ) in the directionally solidified Al-based alloys. Therefore, the purpose of the present work is to investigate the microstructural and microhardness properties of directionally solidified Al–5.5 Zn–2.5Mg ternary alloy depending on the growth rate and effect of microstructures on the microhardness, and relationships between the microstructural and mechanical properties were characterized by linear regression analysis.

## II. EXPERIMENTAL PROCEDURE

### A. Alloy Preparation, Directional Solidification, and Measurement of Microstructures

Weighed quantities of Al, Zn, and Mg metals (purity 99.99 pct) in a graphite crucible (170 mm in length, 30 mm inner diameter, and 40 mm outer diameter) were placed in a vacuum melting furnace, and the metals were completely melted, taking into account the phase diagram as shown in Figure 1.<sup>[37]</sup> After allowing time for the melt to become homogeneous, the melt was poured through a funnel into seven alumina crucibles (200 mm in length, 5 mm ID, and 6 mm OD) in a casting furnace whose lower and upper heater temperatures were approximately 50 K and 100 K (323 °C and 373 °C) above the melting point of the alloy, respectively. The molten alloy solidified from bottom to top in the casting furnace. The directional solidification of the produced sample alloy (Al–5.5Zn–2.5 Mg) was performed in Bridgman-type directional solidification furnace (Figure 2). For directional solidification, first K-type thermocouples with 10 mm spacings were inserted into the thin alumina tubes, and then the sample was placed in the sample holder. The thermocouples were connected to the data logger and computer. The sample was then placed in the cold region of the furnace. After the furnace reached the desired temperature, the sample was driven into the hot region of the furnace and thermally stabilized, and then the sample was withdrawn from the hot region to the cold region of the furnace using different synchronizer motors. The alloy was directionally solidified under different growth rates (8.3 to 165  $\mu\text{m/s}$ ) at a constant temperature gradient (5.5 K/mm). After 90 to 100 mm of the sample had solidified, it was quenched in water. Details of the furnace, equipments, alloy preparation, and directional solidification are described elsewhere.<sup>[2]</sup>

For metallographic processes, the longitudinal and the transverse sections of the samples were mounted on a cold-setting epoxy resin. The samples were then ground with 320 to 4000 grit SiC paper and polished with 3 to 0.25  $\mu\text{m}$  diamond pastes. After finishing the polishing process, the microstructure was revealed using chemical etching process (the samples were etched for 15 seconds with 2 mL nitric acid and 95 mL  $\text{H}_2\text{O}$  solution at room temperature). The micrographs of the samples were taken with a Nikon Eclipse MA 100 optical microscope using different objectives. The dendritic spacings ( $\lambda_1$  and  $\lambda_2$ ) were measured with the Adobe Photoshop CS3 program, with the magnification factor taken into account.<sup>[2]</sup> The primary dendrite arm spacings were obtained by measuring the distance between the nearest two dendrites tips (see Figure 3). Two different methods were used to measure the  $\lambda_1$  values on the transverse sections. One of these methods is the triangle method.<sup>[39]</sup> The triangle is formed by joining the three neighboring dendrite centers, and the sides of triangle corresponded to  $\lambda_{1(\text{tr})}$ . In this method, at least 50 to 200  $\lambda_1$  values were measured for each specimen. The other method is the area counting method.<sup>[40]</sup> The values of  $\lambda_{1(\text{ac})}$  were measured on the transverse section

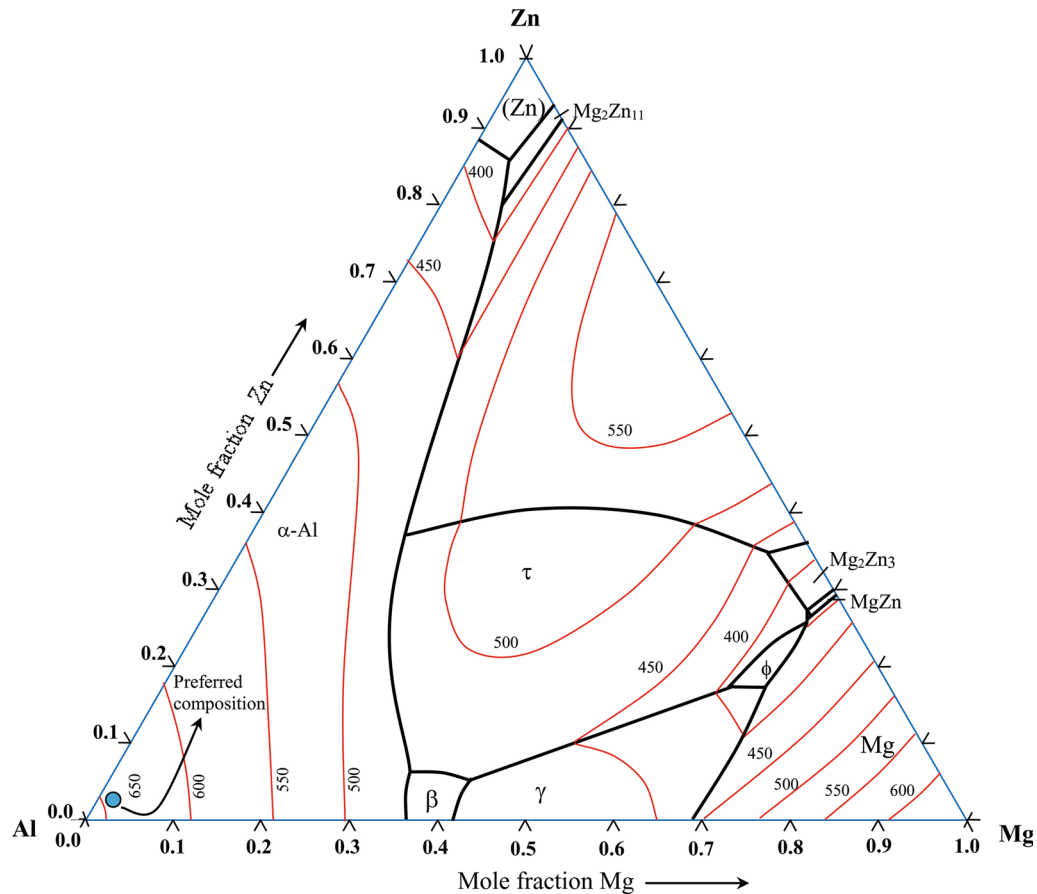


Fig. 1—The ternary Al-Zn-Mg phase diagram (partial).<sup>[37]</sup>

of sample (see Figure 3). In this method the average primary dendrite arm spacings,  $\lambda_{1(ac)}$  were determined from

$$\lambda_{1(ac)} = \frac{1}{M} \left( \frac{N}{A} \right)^{0.5} \quad [12]$$

where  $M$  is the magnification factor,  $A$  is the total sample cross-sectional area, and  $N$  is the number of primary dendrites on the transverse section.  $\lambda_1$  is arithmetic average values of  $\lambda_{1(tr)}$  and  $\lambda_{1(ac)}$ . The secondary dendrite arm spacings,  $\lambda_2$ , were measured from initial adjacent side branches of primary dendrite (see Figure 3). Each of the side-branch spacing data reported here was averaged over the 25 to 50  $\lambda_2$  measurements, depending on the growth conditions.

### B. Measurement of Microhardness (HV)

Microhardness measurements in the present work were made with a DuraScan 20 semiautomatic Microhardness test device using a 300 g load and a dwell time of 10 seconds. Ten measurements were taken from longitudinal and transverse sections of the each sample. The average values were calculated from these microhardness values. Some errors were inevitable during the microhardness measurements. These errors are due to

factors such as surface quality, inhomogeneities in the microstructure, and the ambiguity of the traces. The error in the microhardness measurements has been calculated to be approximately 5 pct.

## III. RESULTS AND DISCUSSION

### A. Composition Analysis of the Phases (WDXRF and EDX Analysis)

As shown in Figures 3 through 5, the solute distributions are not same as in the mushy zone, in the interdendritic (ID), dendrite core (DC), and solid-liquid (S-L) interface region. However, the solid distribution in the liquid, dendrite core, and directionally solidified regions away from the S-L interface are homogeneous.

A composition analysis of the samples was made using a wavelength-dispersive X-ray fluorescence (WDXRF) spectrometry (PANalytical Axios advanced model). As seen in Table I, the nominal composition quantities of Al, Zn, and Mg were found to be 91.94, 5.68, and 2.38 (wt pct), respectively. These values are in agreement with the nominal compositions of the samples.

EDX analysis was performed to determine the composition of the phases in the Al-Zn-Mg ternary alloy at

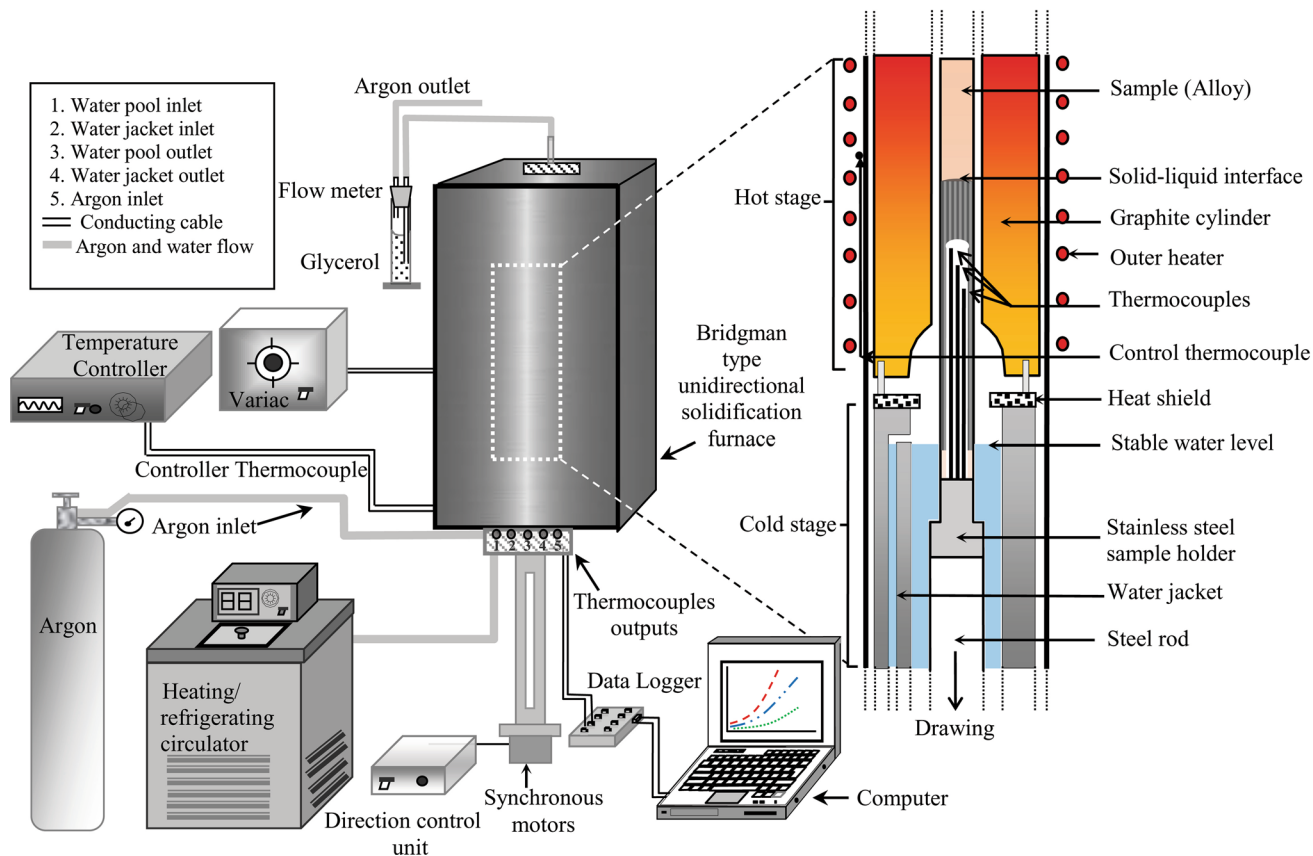


Fig. 2—Bridgman-type directional solidification furnace and its equipments.<sup>[2]</sup>

20 keV using the X-ray lines. According to the EDX analysis results shown in Figure 4, compositions of selected regions in  $\alpha$ -Al and liquid phases were determined as Al-3.09 Zn-0.41 Mg (wt pct) and Al-5.57 Zn-1.45 Mg (wt pct), respectively. As was observed during solidification of the alloy in the  $L + \alpha$  region, the only phase that grew was the  $\alpha$ -Al. In the sample, Zn and Mg contents were measured both on the solid dendrite trunks ( $\alpha$ -Al) and the quenched liquid phases at different points. Zn and Mg contents in the dendrite were determined to be approximately constant, and naturally, these values are lower than the nominal values of the composition because the alloy first starts to solidify with lower composition values, so the dendrite has higher temperatures than the surrounding.<sup>[41]</sup> The solute piles up in front of the dendrite tip at the solid-liquid interface, and then the contents of Zn and Mg were reduced from the solid-liquid interface to liquid phase, and finally, the content of Zn and Mg become closer to the nominal composition (Figure 4).

### B. The Effect of Growth Rate on Dendritic Spacings

The Al-5.5 Zn-2.5 Mg (wt pct) ternary alloy was directionally solidified at the steady-state conditions with different growth rates ( $V = 8.3$ – $165 \mu\text{m/s}$ ) at a constant temperature gradient ( $G = 5.5 \text{ K/mm}$ ). Some optical micrographs of longitudinal and transverse

sections of the directionally solidified Al-Zn-Mg ternary alloy are shown in Figure 5. As shown in Figure 5, the microstructure is usually dendritic in form. Primary and secondary dendrite arms grown in  $\alpha$ -Al phase can be seen clearly. Solidification processing parameters ( $V$ ,  $G$ ,  $C_0$ , and even diameter of the sample) affect the microstructures ( $\lambda_1$ ,  $\lambda_2$ ).<sup>[21–23,39,40,42–51]</sup> Throughout the experiment, all solidification processing parameters, except the growth rates, were kept constant.

The value of  $\lambda_1$  measured in the directionally solidified region is the same as that existing during the growth (in the mushy zone), whereas the secondary spacing is enormously increased due to the contact time between the highly-curved, branched structure and the melt.<sup>[44]</sup> The primary dendritic arm spacings were measured from the longitudinal ( $\lambda_{1L}$ ) and transverse sections ( $\lambda_{1T}$ ) of the samples. Secondary dendritic arm spacings ( $\lambda_2$ ) were measured from the initial adjacent side branches of primary dendrite on the longitudinal sections of the samples.

As can be seen from Figures 6 (a) and (b), an increase in the growth rate caused a decrease of the primary and secondary dendrite arm spacings at a constant temperature gradient ( $5.5 \text{ K/mm}$ ). When the growth rate was increased from  $8.3$  to  $165 \mu\text{m/s}$ , the  $\lambda_{1L}$  value was decreased from  $80.6$  to  $42.5 \mu\text{m}$ , the  $\lambda_{1T}$  value decreased from  $74.8$  to  $36.7 \mu\text{m}$ , and the  $\lambda_2$  value decreased from  $14.3$  to  $7.1 \mu\text{m}$ . As  $\lambda_2$  is reduced, the dendritic structure

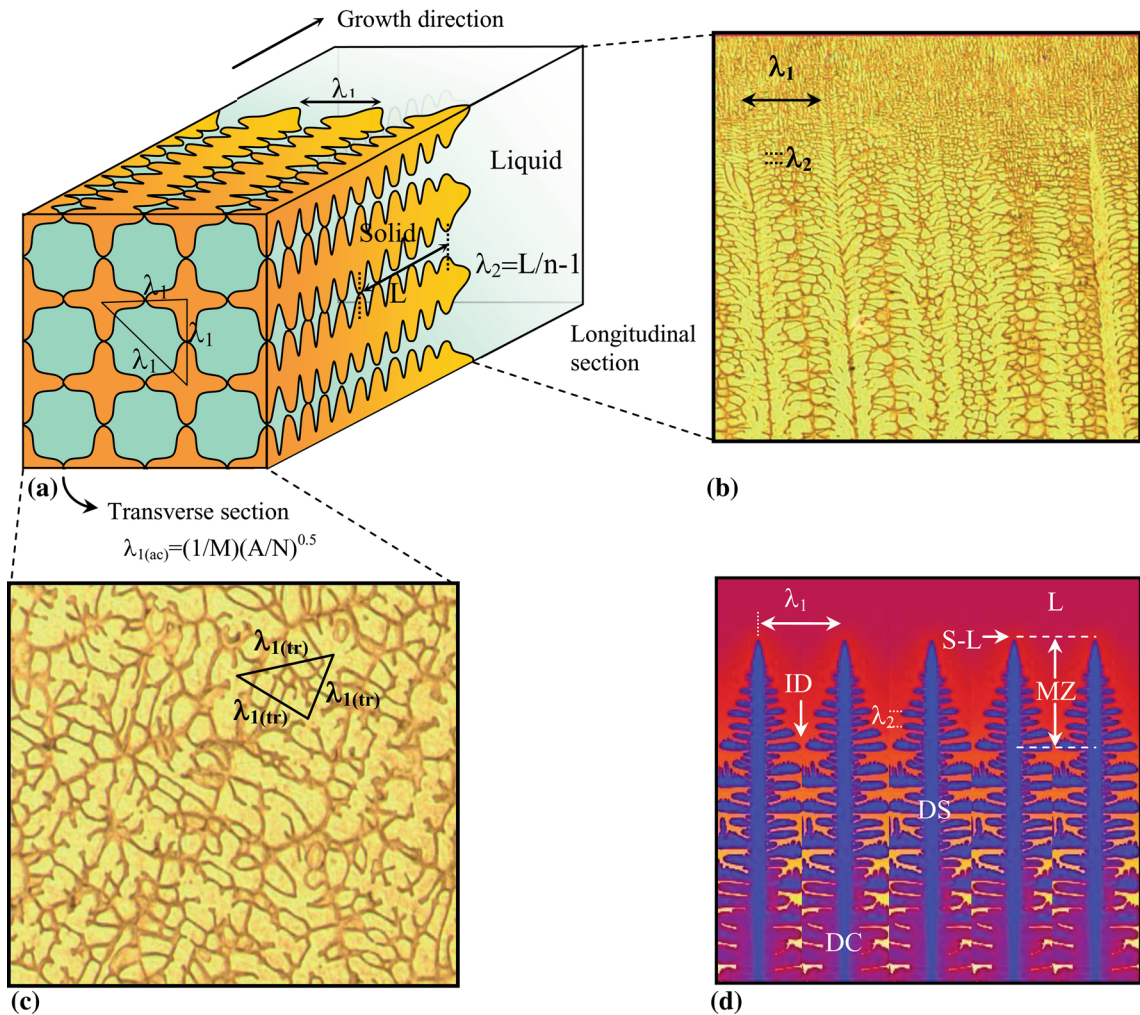


Fig. 3—Schematic illustration of the dendritic spacings measurements (a) perfective illustration of the longitudinal and transverse sections (b) measurements of  $\lambda_1$  and  $\lambda_2$  on the longitudinal section (c) measurement of  $\lambda_1$  with the triangle and area counting methods on the transverse section (d) L: Liquid region; S-L: Solid-liquid interface; MZ: Mushy zone region; DS: Directionally solidified region; ID: Interdendritic region; DC: Dendritic core region (adopted from Ref. [38]).

**Table I. The Identification of Elements from the WDXRF Spectra, Done by a Qualitative Scanning Mode**

Compositions (wt pct)	Error (wt pct)	Crystal	Line	Start at $2\theta$	Finish at $2\theta$
Al (91.94)	0.3	LiF220	$K_\beta$	14.0	18.6
		PX10	$K_\alpha, K_\beta$	11.6	19.0
Zn (5.68)	0.1	LiF220	$L_\beta$	26.2	42.0
		Ge111	$M_\beta$	92.0	146.0
Mg (2.38)	0.05	LiF220	$K_\alpha, K_\beta$	36.4	42.0

becomes cleaner and sounder, and these qualities are important contributors to improved properties.<sup>[51]</sup> A similar observation concerning a commercial Al 7 wt pct Si alloy has also been reported in the literature.<sup>[52,53]</sup>

The dependency of  $\lambda_{1L}$ ,  $\lambda_{1T}$ , and  $\lambda_2$  on  $V$  was determined by a linear regression analysis. From the experimental results, the relationships between dendritic spacings and growth rate are shown in Figure 6 and Table II. The exponent values of  $V$  for  $\lambda_{1L}$ ,  $\lambda_{1T}$ , and  $\lambda_2$  in the directionally solidified Al-Zn-Mg ternary alloy were found to be 0.20, 0.24, and 0.22, respectively. The

exponent values (0.20 and 0.24) of  $V$  for  $\lambda_{1L}$  and  $\lambda_{1T}$  obtained in this work are in agreement with the values of 0.25, 0.26, 0.25, and 0.28 reported by Gündüz *et al.*<sup>[45]</sup> for Al-0.5Ti (wt pct) alloy, by Berkdemir and Gündüz<sup>[46]</sup> for Al-5Cu-3Mg (wt pct) alloy, by Kaya *et al.*<sup>[47]</sup> for Al-2Li (wt pct) alloy, and by McCartney and Hunt<sup>[48]</sup> for Al-0.15Mg-0.33 Si (at. pct) alloy, respectively. The exponent value of  $V$  (0.22) for  $\lambda_2$  is slightly lower than the values of 0.32 and 0.38 reported by Berkdemir and Gündüz<sup>[46]</sup> for Al-5Cu-3Mg (wt pct) alloy and by Tunca and Smith<sup>[49]</sup> for Al-8 Zn alloy (wt pct), respectively.

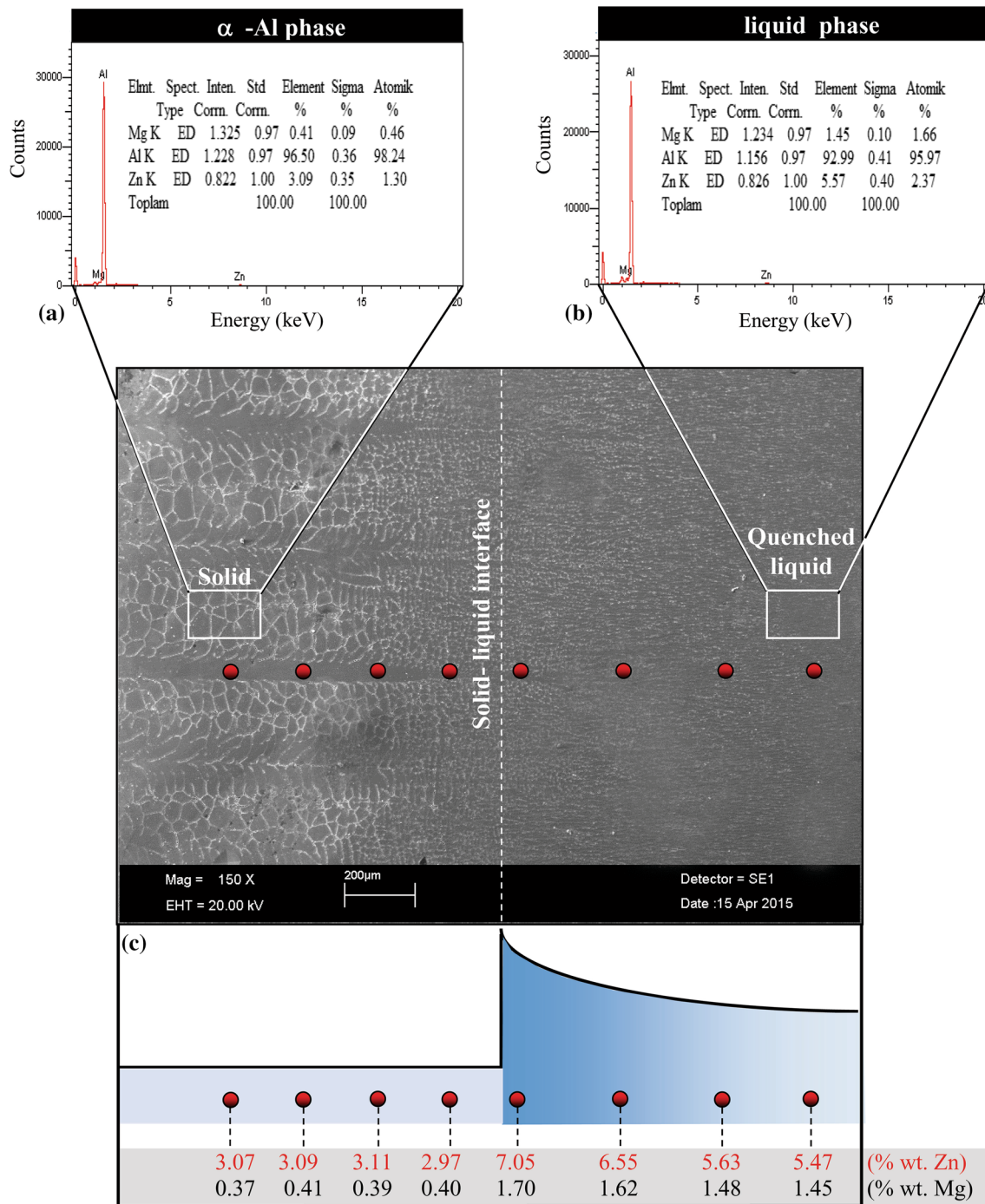


Fig. 4—The chemical composition analysis of the Al-5.5 Zn-2.5 Mg ternary alloy (a) spectrum of  $\alpha$ -Al phase (b) spectrum of liquid phase (c) solute distributions in  $\alpha$ -Al matrix phase.

The experimental exponent values (0.20, 0.24) of  $V$  for  $\lambda_{1L}$  and  $\lambda_{1T}$  are also in agreement with the theoretical value (0.25) of Hunt,<sup>[21]</sup> Trivedi,<sup>[22]</sup> Kurz-Fisher,<sup>[23]</sup> Laxmanan,<sup>[50]</sup> and Ma-Sahm<sup>[51]</sup> models for steady-state conditions.

The experimental exponent value (0.22) of  $V$  for  $\lambda_2$  is lower than the theoretical exponent values (0.50, 0.66) of the Trivedi-Soomboonsuk<sup>[25]</sup> and Bouchard-Kirkaldy<sup>[26]</sup> models, respectively. The theoretical and numerical models are generally based on binary dilute

alloys and limited growth rates and temperature gradients, so the discrepancies between the experimental and theoretical values might be due to the compositions, temperature gradients, and sample sizes.

### C. The Effect of Dendritic Spacing and Growth Rate on Microhardness

As can be seen from Figure 6, as the growth rate increases, microstructures ( $\lambda_1$ ,  $\lambda_2$ ) decrease. Similarly, as

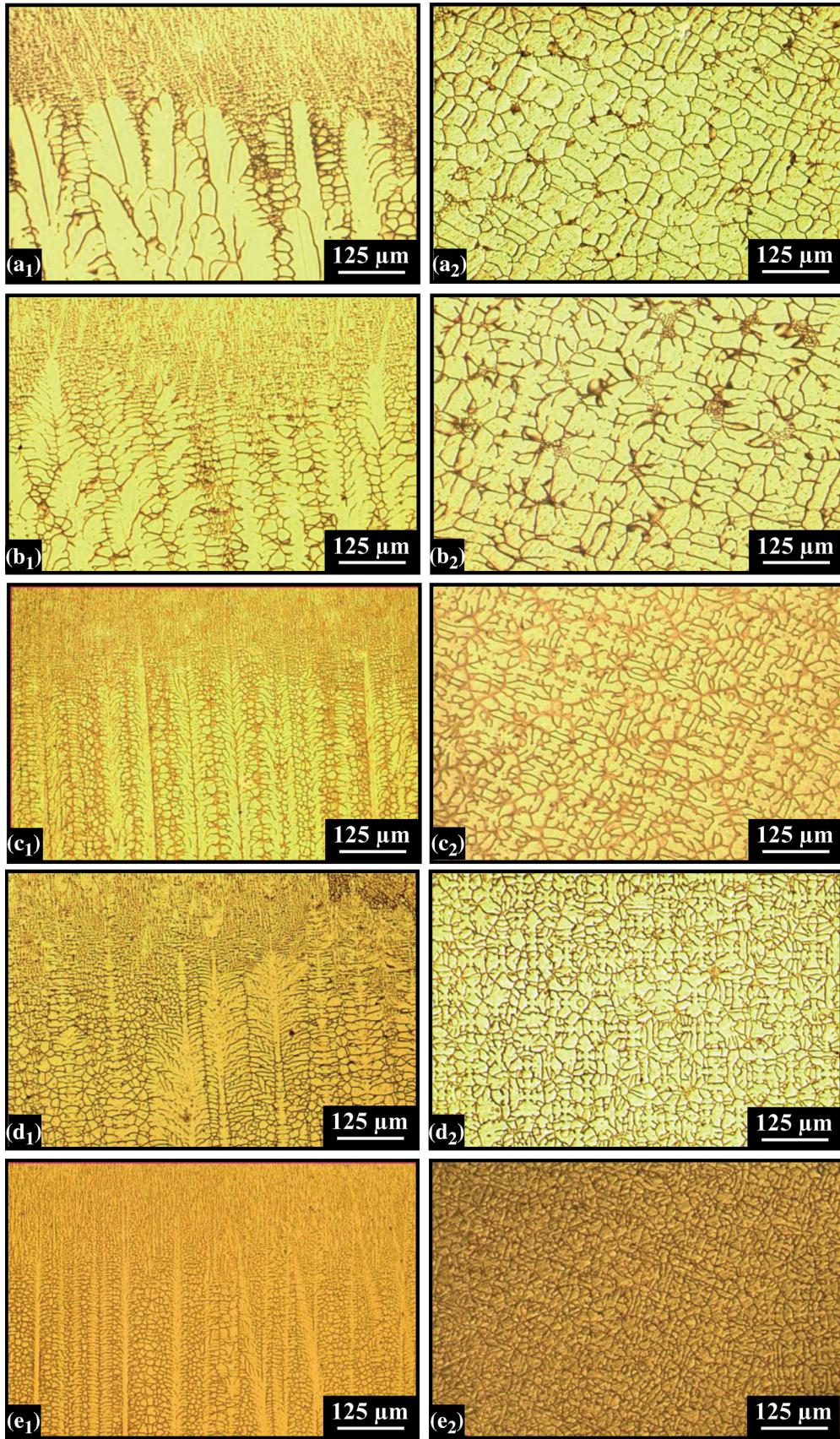




Fig. 5—Some optical images of the directionally solidified Al-5.5 Zn-2.5 Mg ternary alloy at a constant temperature gradient (5.5 K/mm), different growth rates ( $V = 8.3\text{--}165\ \mu\text{m/s}$ ) ( $a_1$ ) longitudinal section ( $a_2$ ) transverse section ( $V = 8.3\ \mu\text{m/s}$ ), ( $b_1$ ) longitudinal section ( $b_2$ ) transverse section ( $V = 16.5\ \mu\text{m/s}$ ), ( $c_1$ ) longitudinal section ( $c_2$ ) transverse section ( $V = 41.2\ \mu\text{m/s}$ ) ( $d_1$ ) longitudinal section ( $d_2$ ) transverse section ( $V = 82.5\ \mu\text{m/s}$ ) ( $e_1$ ) longitudinal section ( $e_2$ ) transverse section ( $V = 165\ \mu\text{m/s}$ ).

the microstructures of the Al-Zn-Mg alloy decrease, the microhardness of the alloy increases (Figure 7). As can be seen from the results of experimental works, and theoretical and numerical models, microstructure size ( $\lambda_1, \lambda_2$ ) is more effective than the growth rate on microhardness. The dependencies of microhardness on the growth rate are shown in Figure 8, and the

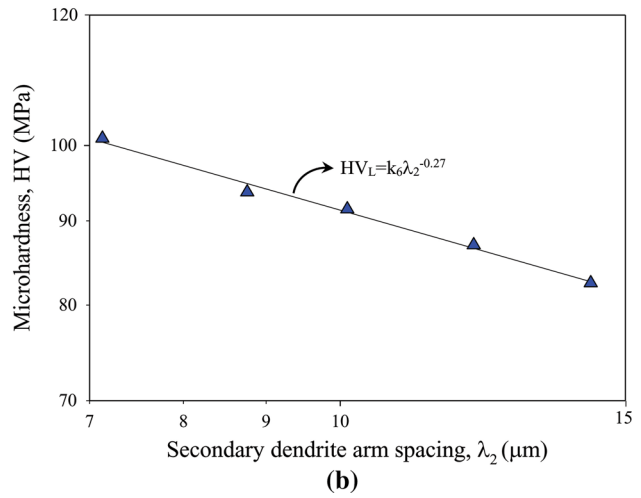
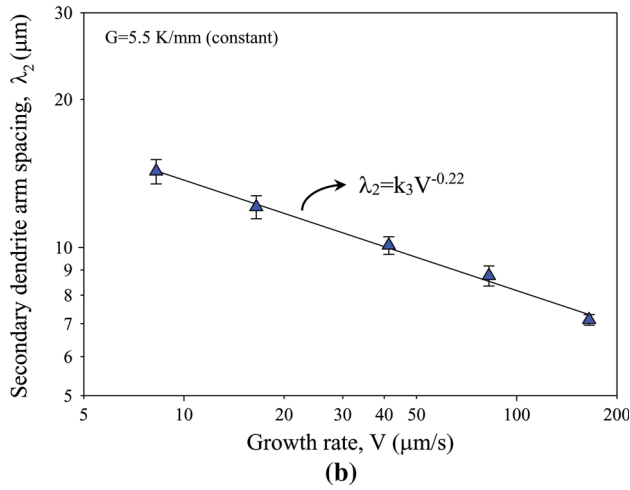
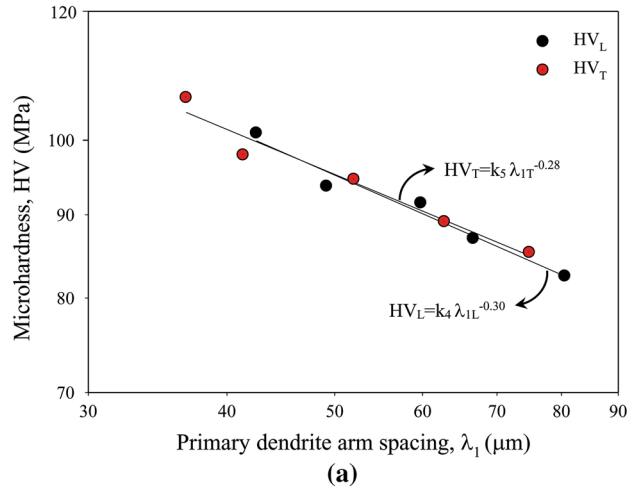
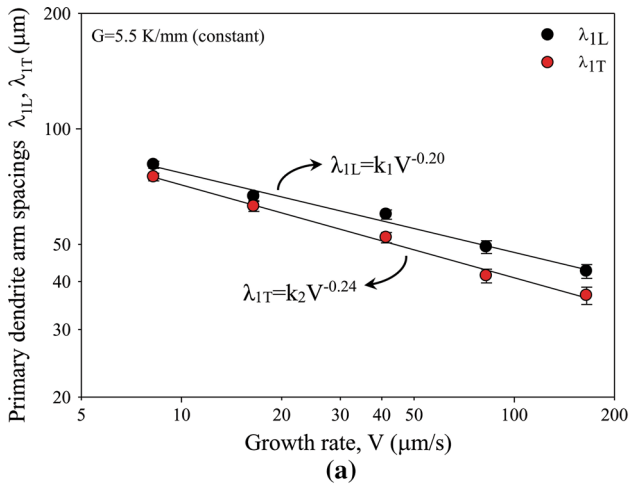


Fig. 6—The variation of dendritic spacings with growth rate at a constant temperature gradient (a)  $\lambda_1$  vs  $V$  (b)  $\lambda_2$  vs  $V$ .

Fig. 7—The variation of microhardness with dendritic spacings at a constant temperature gradient (a)  $HV$  vs  $\lambda_1$  (b)  $HV$  vs  $\lambda_2$ .

Table II. The Relationships Between the Microstructure Parameters, Growth Rate, and Microhardness

Relationships	Constant ( $k$ )	Correlation Coefficient ( $r$ )
$\lambda_{1L} = k_1 V^{-0.20}$	$k_1 = 123\ \mu\text{m}^{1.20}\ \text{s}^{-0.20}$	$r_1 = -0.985$
$\lambda_{1T} = k_2 V^{-0.24}$	$k_2 = 123\ \mu\text{m}^{1.24}\ \text{s}^{-0.24}$	$r_2 = -0.993$
$\lambda_2 = k_3 V^{-0.22}$	$k_3 = 23\ \mu\text{m}^{1.22}\ \text{s}^{-0.22}$	$r_3 = -0.989$
$HV_L = k_4 \lambda_{1L}^{-0.30}$	$k_4 = 301\ \text{MPa}\ \mu\text{m}^{0.30}$	$r_4 = -0.934$
$HV_T = k_5 \lambda_{1T}^{-0.28}$	$k_5 = 289\ \text{MPa}\ \mu\text{m}^{0.28}$	$r_5 = -0.978$
$HV_L = k_6 \lambda_2^{-0.27}$	$k_6 = 170\ \text{MPa}\ \mu\text{m}^{0.27}$	$r_6 = -0.982$
$HV_L = k_7 V^{0.06}$	$k_7 = 70\ \text{MPa}\ \mu\text{m}^{-0.06}\ \text{s}^{-0.06}$	$r_7 = 0.974$
$HV_T = k_8 V^{0.07}$	$k_8 = 73\ \text{MPa}\ \mu\text{m}^{-0.07}\ \text{s}^{-0.07}$	$r_8 = 0.989$

$\lambda_{1L}$ , the average values of the primary dendrite arm spacing measured from the longitudinal section of the samples.  $\lambda_{1T}$ , the average values of the primary dendrite arm spacing measured from the transverse section of the samples.  $HV_L$ , the average values of the microhardness measured from the longitudinal section of the samples.  $HV_T$ , the average values of the microhardness measured from the transverse section of the samples.

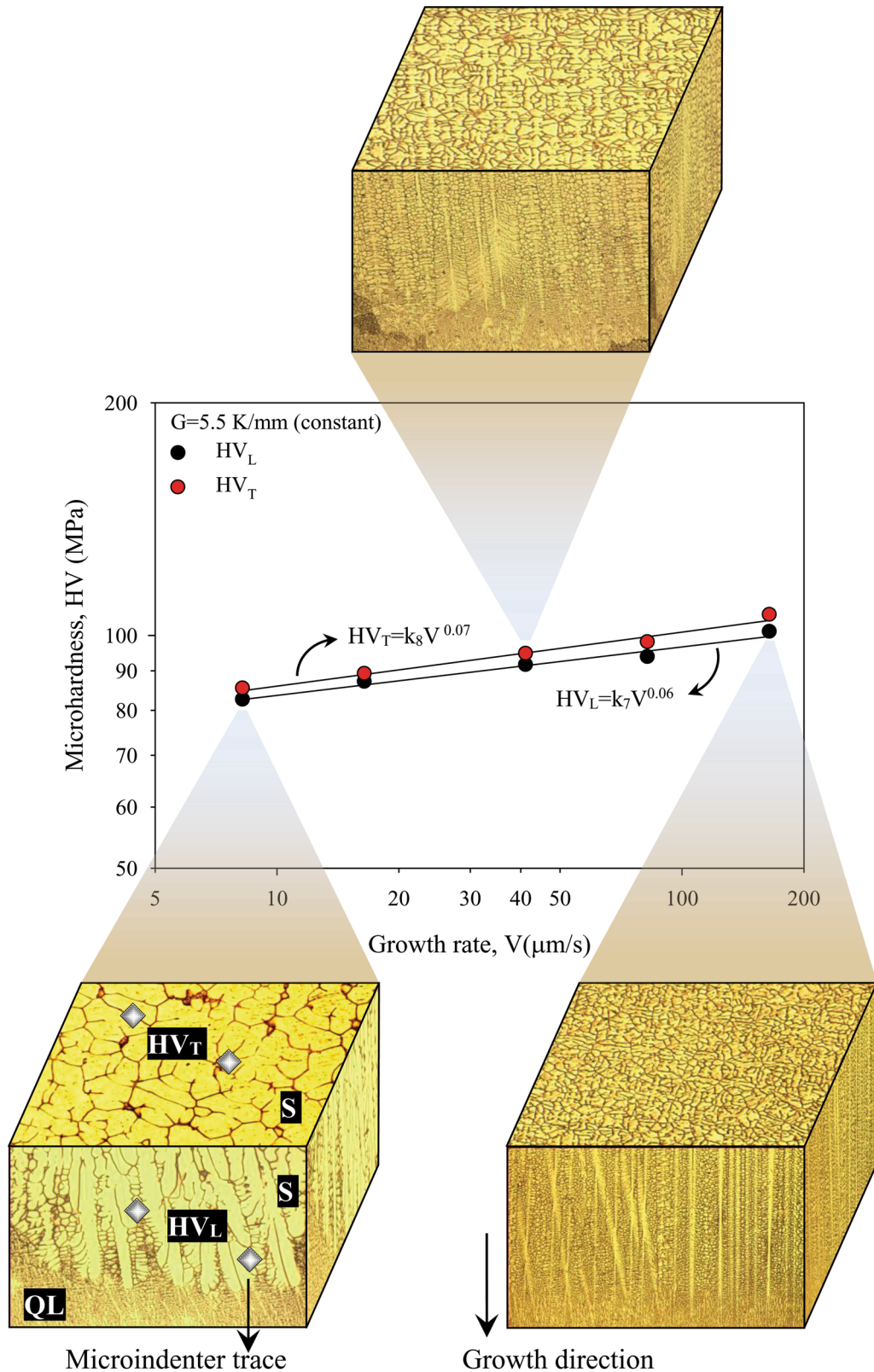


Fig. 8—The variation of microhardness with growth rate at a constant temperature gradient (S: solid, QL: quenched liquid).

relationships between these parameters are shown in Table II. As can be seen from Figure 8, at a constant temperature gradient (5.5 K/mm), an increase in growth

rate results in an increase in microhardness. When the growth rate was increased from 8.3 to 165  $\mu\text{m/s}$ ,  $\lambda_1$  and  $\lambda_2$  decreased from 80.6 and 14.3  $\mu\text{m}$  to 42.5 and 7.1  $\mu\text{m}$

respectively. Thereupon,  $HV_L$  and  $HV_T$  increased from 82.5 and 85.3 MPa to 101 and 106.2 MPa, respectively.

The dependency of  $V$ ,  $\lambda_1$ , and  $\lambda_2$  on HV was determined by a linear regression analysis. The relationships between growth rate, dendritic spacings, and microhardness are shown in Figures 6 and 7, and Table II. The exponent values of  $V$ ,  $\lambda_{1L}$ ,  $\lambda_{1T}$ , and  $\lambda_2$  for HV in the directionally solidified Al-Zn-Mg ternary alloy were found to be 0.07, 0.30, 0.28, and 0.27, respectively. The exponent value of  $V$  (0.07) obtained from this study as a function of HV is in agreement with the values of 0.06, 0.06, 0.04, 0.07, 0.07, 0.07, and 0.07 values reported by Çadırlı *et al.*<sup>[54]</sup> for Sn-23Bi-5Zn (wt pct) alloy, Hu *et al.*<sup>[55]</sup> for Sn-58 wt pct Bi alloy, by Guo *et al.*<sup>[56]</sup> for NiAl-28Cr-5Mo-1Hf (at. pct) alloy, by Vnuk *et al.*<sup>[57]</sup> for Sn-Zn alloy, by Lapin and Marecek<sup>[58]</sup> for Ni-21.9Al-8.1Cr-4.2Ta-0.9Mo-0.3Zr alloy (at. pct), by Büyük *et al.*<sup>[59]</sup> for Zn-7Al-4Cu (wt pct) alloy, and Kaya *et al.*<sup>[60]</sup> for Al-based alloys (Al-0.1 wt pct Ti, Al-0.5 wt pct Ti and Al-2 wt pct Li), respectively. The exponent value of  $V$  (0.07) for HV is lower than the values of 0.11, 0.14, and 0.15 reported by Hu *et al.*<sup>[61]</sup> for Sn-1.0 wt pct Cu, by Lapin *et al.*<sup>[62]</sup> for Ti-46Al-2W-0.5Si (at. pct) alloy, and by Fan *et al.*<sup>[63]</sup> for Ti-46Al-0.5W-0.5Si alloy (at. pct), respectively. The average exponent value of  $\lambda_1$  (0.29) obtained in this study as a function of the HV is slightly higher than the values of 0.22, 0.24, 0.21, 0.20, 0.25, and 0.28 reported by Büyük *et al.*<sup>[64]</sup> for Al-17.6Cu-42.2Ag (wt pct) alloy, by Engin *et al.*<sup>[65]</sup> for Zn-5 wt pct Al alloy, by Hu *et al.*<sup>[61]</sup> for Sn-1.0 wt pct Cu alloy, by Hu *et al.*<sup>[66]</sup> for Sn-40.5Pb-2.6Sb (wt pct) alloy, by Kaya *et al.*<sup>[60]</sup> for Al-0.1 wt pct Ti alloy, and by Kaya *et al.*<sup>[67]</sup> for Al-3 wt pct Si alloy, respectively. Also, the exponent value (0.27) of  $\lambda_2$  in this work is in agreement with the values 0.22, 0.25, and 0.24 obtained by Khan *et al.*<sup>[68]</sup> for Al-Si alloy and by Kaya *et al.*<sup>[67,69]</sup> for Al-3 wt pct Si and Al-7 wt pct Ni alloy, respectively, for similar solidification conditions. Hu *et al.*<sup>[70]</sup> show that the exponent of growth rate decreases with decreasing the sample diameter because the smaller-diameter sample reduces the convection and would be allow to obtain a diffusive growth condition. As seen in the results, even though experiments were conducted under similar conditions (samples with the similar compositions, growth rate, and temperature gradient), experiments can give discrepancies in the results. This is because not only the growth rate, temperature gradient, and composition of the sample but also anisotropy of the solid-liquid interfacial energy, molecular attachment kinetic,<sup>[71]</sup> changing the growth directions,<sup>[72]</sup> convections,<sup>[70,73]</sup> ripening process,<sup>[74]</sup> the size, impurities, preparation (as-cast, extruded, *etc.*), and heating and cooling rates of the sample affect the microhardness.<sup>[75-81]</sup>

#### IV. CONCLUSIONS

In this work, directional solidification experiments have been carried out with an Al-5.5Zn-2.5Mg alloy in order to see the effect of growth rate  $V$  on the dendritic spacings and microhardness. Effects of dendrite spacings

on microhardness were also examined. The results are summarized as follows:

1. Experimental observations show that the values of  $\lambda_1$  and  $\lambda_2$  decrease as  $V$  increases. The relationships between microstructure parameters ( $\lambda_1$  and  $\lambda_2$ ) and the growth rate have been obtained as  $\lambda_{1L} = k_1 V^{-0.20}$ ,  $\lambda_{1T} = k_2 V^{-0.24}$  and  $\lambda_2 = k_3 V^{-0.22}$ .
2. Increasing of the growth rate resulted in finer dendritic microstructures, thereby resulting in increased microhardness. The establishment of the relationships among  $HV_L$ ,  $HV_T$ ,  $V$ ,  $\lambda_{1L}$ ,  $\lambda_{1T}$ , and  $\lambda_2$  have been obtained as  $HV_L = k_4 \lambda_{1L}^{-0.30}$ ,  $HV_T = k_5 \lambda_{1T}^{-0.28}$ ,  $HV_L = k_6 \lambda_2^{-0.27}$ ,  $HV_L = k_7 V^{0.06}$ , and  $HV_T = k_8 V^{0.07}$ .

#### ACKNOWLEDGMENTS

This project was supported by the Erciyes University Scientific Research Project Unit under contract No: FBD-12-3978. The authors are grateful for this financial support.

#### REFERENCES

1. I. Polmear: *Light alloys: From Traditional Alloys to Nanocrystals*, Butterworth-Hinemann, 4th ed., London, 2005.
2. M. Gündüz and E. Çadırlı: *Mater. Sci. Eng. A.*, 2002, vol. 327, pp. 167–85.
3. R. Ghiaasiaan, X. Zeng, and S. Shankar: *Mater. Sci. Eng. A.*, 2014, vol. 594, pp. 260–77.
4. L.M. Wu, W.H. Wang, Y.F. Hsu, and S. Trong: *J. Alloys Compd.*, 2008, vol. 56, pp. 163–69.
5. S. Guo, Z.L. Ning, M.X. Zhang, F.Y. Cao, and J.F. Sun: *Mater. Charact.*, 2014, vol. 87, pp. 62–69.
6. Y.L. Deng, Y.Y. Zhang, L. Wan, A.A. Zhu, and X.M. Zhang: *Metall. Mater. Trans. A*, 2013, vol. 44A, pp. 2470–77.
7. B.I. Jung, C.H. Jung, T.K. Han, and Y.H. Kim: *J. Mater. Process. Technol.*, 2001, vol. 111, pp. 69–73.
8. X. Jian, H. Xu, T.T. Meek, and Q. Han: *Mater. Lett.*, 2005, vol. 59, pp. 190–93.
9. E. Çadırlı, H. Kaya, D. Rabiger, S. Eckert, and M. Gündüz: *J. Alloys Compd.*, 2015, vol. 647, pp. 471–80.
10. J. Wang, S. He, B. Sun, Q. Guo, and M. Nishio: *J. Mater. Process. Technol.*, 2003, vol. 141, pp. 29–34.
11. H. Liao, Y. Sun, and G. Sun: *Mater. Sci. Eng. A.*, 2002, vol. 335, pp. 62–66.
12. E.J. Abed: *Int. J. Eng. Technol.*, 2011, vol. 11, pp. 34–44.
13. D.A. Porter and K.E. Easterling: *Phase Transformation in Metals and Alloys*, 2nd ed., Chapman and Hall, London, 1992.
14. E.J. Lavernia, J.D. Ayers, and T.S. Srivatsan: *Int. Mater. Rev.*, 1992, vol. 37, pp. 1–44.
15. E. Çadırlı: *Met. Mater. Int.*, 2013, vol. 19, pp. 411–22.
16. M.H. Avazkonandeh-Gharavol, M. Haddad-Sabzevar, and H. Fredriksson: *J. Alloys Compd.*, 2014, vol. 610, pp. 462–71.
17. F. Yang, L. Peng, and K. Okazaki: *Metall. Mater. Trans. A*, 2004, vol. 35A, pp. 3323–28.
18. W.R. Osório, L.C. Peixoto, M.V. Canté, and A. Garcia: *Mater. Design*, 2010, vol. 31, pp. 4485–89.
19. H. Kaya, E. Çadırlı, M. Gündüz, and A. Ülgen: *J. Mater. Eng. Perform.*, 2003, vol. 12, pp. 544–51.
20. K.S. Cruz, E.S. Meza, F.A.P. Fernandes, J.M.V. Quaresma, L.C. Casteletti, and A. Garcia: *Metall. Mater. Trans. A*, 2010, vol. 41A, pp. 972–84.
21. J.D. Hunt: *Solidification and Casting of Metals*, The Metal Society, London, 1979.

22. R. Trivedi: *Metall. Trans. A*, 1984, vol. 15A, pp. 977–82.
23. W. Kurz and D.J. Fisher: *Acta Metall.*, 1981, vol. 29, pp. 11–20.
24. T. Okamoto and K. Kishitake: *J. Cryst. Growth*, 1975, vol. 29, pp. 137–46.
25. R. Trivedi and K. Somboonsuk: *Mater. Sci. Eng.*, 1984, vol. 65, pp. 65–74.
26. E. Bouchard and J.S. Kirkaldy: *Metall. Mater. Trans. B*, 1997, vol. 28, pp. 651–63.
27. W.W. Mullins and R.F. Sekerka: *J. Appl. Phys.*, 1964, vol. 35, pp. 444–51.
28. E.O. Hall: *Proc. Phys. Soc. (Lond.)*, 1951, vol. 64B, pp. 747–53.
29. N.J. Petch: *J. Iron Steel Inst.*, 1953, vol. 174, pp. 25–28.
30. W.R. Osorio and A. Garcia: *Mater. Sci. Eng. A*, 2002, vol. 325, pp. 103–11.
31. W. Blum, Y.J. Li, J. Chen, X.H. Zeng, and K. Lu: *Int. J. Mater. Res.*, 2006, vol. 97, pp. 1661–66.
32. H. Sun and Y. Shi: *J. Mater. Sci. Technol.*, 2009, vol. 25, pp. 347–50.
33. C.E. Carlton and P.J. Ferreira: *Acta Mater.*, 2007, vol. 55, pp. 3749–56.
34. A. Munitz: *Metall. Trans. B*, 1985, vol. 16, pp. 149–61.
35. M. Zimmermann, M. Carrard, and W. Kurz: *Acta Metall.*, 1989, vol. 37, pp. 3305–13.
36. C.D. Lee: *Mater. Sci. Eng. A*, 2007, vol. 459, pp. 355–60.
37. D.A. Petrov: in *Ternary Alloys*, G. Petzow and G.E. Effenberg, eds., VCH, Weinheim, 1986.
38. R. Shao: Ph.D. thesis, Purdue University, West Lafayette, IN, 2007.
39. S. Ganesan, C.L. Chan, and D.R. Poirier: *Mater. Sci. Eng. A*, 1992, vol. 151, pp. 97–105.
40. M.S. Bhat, D.R. Poirier, and J.C. Heinrich: *Metall. Mater. Trans. B*, 1995, vol. 26, pp. 1049–56.
41. Z. Chen, Y. Mo, and Z. Nie: *Metall. Mater. Trans. A*, 2013, vol. 44A, pp. 3910–20.
42. L. Lasa and J.M. Rodrigues-Ibade: *Mater. Sci. Eng. A*, 2003, vol. 363, pp. 193–202.
43. C. Brito, T.A. Costa, T.A. Vida, F. Bertelli, N. Cheung, J.E. Spinelli, and A. Garcia: *Metall. Mater. Trans. A*, 2015, vol. 46A, pp. 3342–55.
44. W. Kurz and D.J. Fisher: *Fundamentals of Solidification*, Trans. Tech. Publications, Aedermannsdorf, Switzerland, 1989.
45. M. Gündüz, H. Kaya, E. Çadırlı, N. Maraşlı, K. Keşioğlu, and B. Saatçi: *J. Alloys Compd.*, 2007, vol. 439, pp. 114–27.
46. A. Berkdemir and M. Gündüz: *Mater. Sci. Forum*, 2010, vol. 649, pp. 425–30.
47. H. Kaya, E. Çadırlı, and M. Gündüz: *Appl. Phys. A*, 2009, vol. 94, pp. 155–65.
48. D.G. McCartney and J.D. Hunt: *Acta Mater.*, 1981, vol. 29, pp. 1851–63.
49. H. Tunca and R.W. Smith: *J. Mater. Sci.*, 1988, vol. 23, pp. 111–20.
50. V. Laxmanan: *Acta Metall.*, 1985, vol. 33, pp. 1023–35.
51. D. Ma and P.R. Sahn: *Metall. Mater. Trans. A*, 1998, vol. 29A, pp. 1113–19.
52. J. Campbell: *Castings*, Butterworth-Heinemann, Oxford, UK, 1991.
53. E.L. Rooy: *Metals Handbook*, Castings, ASM International, Metals Park, OH, 1988, vol. 15.
54. E. Çadırlı, U. Büyük, H. Kaya, and N. Maraşlı: *J. Non Cryst. Solids*, 2011, vol. 357, pp. 2876–81.
55. X. Hu, K. Li, and F. Ai: *China Foundry*, 2012, vol. 9, pp. 360–65.
56. J.T. Guo, C.M. Xu, X.H. Du, and H.Z. Fu: *Mater. Lett.*, 2004, vol. 58, pp. 3233–36.
57. F. Vnuk, M. Sahoo, D. Baragor, and R.W. Smith: *J. Mater. Sci.*, 1980, vol. 15, pp. 2573–83.
58. J. Lapin and J. Marecek: *Intermetallics*, 2006, vol. 14, pp. 1339–44.
59. U. Büyük, S. Engin, and N. Maraşlı: *J. Min. Metall. Sect. B*, 2015, vol. 51, pp. 67–72.
60. H. Kaya, M. Gündüz, E. Çadırlı, and N. Maraşlı: *J. Alloys Compd.*, 2009, vol. 478, pp. 281–86.
61. X. Hu, W. Chen, and B. Wu: *Mater. Sci. Eng. A*, 2012, vol. 556, pp. 816–23.
62. J. Lapin, L. Ondrus, and M. Nazmy: *Intermetallics*, 2002, vol. 10, pp. 1019–31.
63. J. Fan, X. Li, Y. Su, J. Guo, and H. Fu: *J. Alloy Compd.*, 2010, vol. 504, pp. 60–64.
64. U. Büyük, N. Maraşlı, E. Çadırlı, H. Kaya, and K. Keşioğlu: *Curr. Appl. Phys.*, 2012, vol. 12, pp. 7–10.
65. S. Engin, U. Büyük, H. Kaya, and N. Maraşlı: *Int. J. Miner. Met. Mater.*, 2011, vol. 18, pp. 659–64.
66. X.W. Hu, S.M. Li, S.F. Gao, L. Liu, and H.Z. Fu: *J. Alloy Compd.*, 2010, vol. 493, pp. 116–21.
67. H. Kaya, E. Çadırlı, U. Büyük, and N. Maraşlı: *App. Surf. Sci.*, 2008, vol. 255, pp. 3071–78.
68. S. Khan, A. Ourdjini, Q.S. Hamed, M.A.A. Najafabadi, and R. Elliott: *J. Mater. Sci.*, 1993, vol. 28, pp. 5957–62.
69. H. Kaya, U. Büyük, E. Çadırlı, and N. Maraşlı: *Met. Mater. Int.*, 2013, vol. 19, pp. 39–44.
70. X.W. Hu, S.M. Li, S.F. Gao, L. Liu, and H. Fu: *Trans. Nonferr. Met. Soc. China*, 2011, vol. 21, pp. 65–71.
71. M.E. Gliksmann, R.J. Schaefer, and J.D. Ayers: *Metall. Trans. A*, 1976, vol. 7A, pp. 1747–59.
72. S. Henry, T. Minghetti, and M. Rappaz: *Acta Mater.*, 1998, vol. 46, pp. 6431–43.
73. L. Yu, G.L. Ding, J. Reye, S.N. Ojha, and S.N. Tewari: *Metall. Mater. Trans. A*, 2000, vol. 31A, pp. 2275–85.
74. J. Zhang, X. Ma, H. Ren, L. Chen, Z. Jin, Z. Li, and J. Shen: *JOM*, 2016, vol. 68, pp. 178–84.
75. J.W. Martins: *Precipitation Hardening*, 2nd ed., Butterworth-Heinemann, Oxford, UK, 1998.
76. H. Tecer: Ph.D. thesis, Erciyes University, Kayseri, Turkey, 2013.
77. H. Li, J. Bin, J. Liu, Z. Gao, and X. Lu: *Scripta Mater.*, 2012, vol. 67, pp. 73–76.
78. T.T. Sasaki, K. Oh-ishi, T. Ohkubo, and K. Hono: *Mater. Sci. Eng. A*, 2011, vol. 530, pp. 1–8.
79. S.P. Ringer and K. Hono: *Mater. Charact.*, 2000, vol. 44, pp. 101–31.
80. O. El Sebaie, A.M. Samuel, F.H. Samuel, and H.W. Doty: *Mater. Sci. Eng. A*, 2008, vol. 480, pp. 342–55.
81. D.D. Risanti, M. Yin, P.E.J.R.D. Castillo, and S. Vau der Zwang: *Mater. Sci. Eng. A*, 2009, vol. 523, pp. 99–111.